Scale invariance of mechanical properties in the developing mammalian retina

Elijah Robinson Shelton[1], Michael Frischmann[1], Achim Theo Brinkop[1], Rebecca Marie James[1,2], Friedhelm Serwane[1,3,4*]

[1]Faculty of Physics and Center for NanoScience (CeNS), Ludwig-Maximilians-University, Munich, Germany.
[2]Present address: Institute of Neuronal Cell Biology, Technical University of Munich Munich, Germany.
[3]Graduate School of Systemic Neuroscience (GSN), Ludwig-Maximilians-University,, Munich, Germany.
[4]Munich Cluster for Systems Neurology (SyNergy), Munich, Germany.

*Corresponding author(s). E-mail(s): f.serwane@lmu.de;

Abstract

Neuronal tissues form through physical forces guiding neuron movements. In the mammalian retina, events like neuron translocation occur over hours. How mechanical stresses induce tissue organisation at this timescale has remained unclear due to the inaccessibility of living retina tissue for *in situ* mechanical interrogation. Previous studies captured responses at second timescales or shorter. Here, we probed tissue mechanics in an *in vitro* model of the developing retina using magnetic droplets in mouse stem cell-derived retina organoids. We recorded strain responses to stress across four orders of magnitude in time, up to one hour. Dynamic creep compliance and tensile moduli followed a power law with an exponent consistent with a material just above the glass transition. Our findings suggest that neuronal tissue remodels in a scale-free manner while maintaining solid-like properties. Our measurements could open the door to understanding how mechanical signals drive connectivity in the central nervous system.

Keywords: Neuroepithelium, Retina, Mechanical properties, Ferrofluid droplets, Organoid, Mechanics, Power Law, Soft glassy rheology

1 Introduction

Mechanical forces, alongside biochemical factors, drive both large-scale and local structural remodeling within the developing central nervous system (CNS)[1–3]. The retina is a prime example, transforming from a neuroepithelium into a layered, light-sensitive neuronal tissue. It has become a focal point for researchers investigating the links between tissue organization, molecular factors, and cellular forces[4, 5]. In addition to cellular forces, the material properties of the neuron's environment determine how a neuron translocates during retinogenesis and whether it ultimately arrives at its designated position within the tissue. However, it is experimentally difficult to quantify this constitutive relation between force and displacement during retinogenesis as it requires the application of a (i) known force *in situ* (ii) over the course of retina neuron translocation taking minutes to hours. On a shorter timescale, elastic responses have been measured and reported for living guinea pig and ruminant retinae slices using the atomic force microscope (AFM)[6, 7], and the mechanics at nanosecond actuation periods have been mapped for the mouse retina using Brillouin microscopy[8]. Discrepancies between AFM and Brillouin microscopy measurements have been observed and could be attributed to differences in length and timescale of the mechanical stimulation[8]. This highlights the importance of characterizing the mechanics at timescales relevant to the process under study[9, 10]. In the case of the retina, and neuronal tissue more generally, measurements of the mechanical properties at the minutes to hours timescales of retinogenesis are sparse[3, 11, 12].

Recently, stem cell-derived *in vitro* organoid models have provided researchers with systems which complement traditional animal models as platforms for studying the details of retina development. Termed retina organoids[5, 13], these model systems display all cell types and mimic the tissue architecture of the *in vivo* retina[14–16]. In both *in vitro* and *in vivo* systems, retina development starts with an ensemble of neural progenitor cells derived from embryonic stem cells (ESCs)[14, 17]. Parts of the ensemble transform into a single layer neuroepithelium which then becomes the neural retina[14, 17]. At this stage, researchers have measured the elastic properties of its surface using an AFM on mouse retina organoids[14]. The results have served as inputs for mechanical modelling using vertex models[14, 18, 19] and successfully explained the morphological changes the neuroepithelium undergoes before it starts converting into a 3D laminated tissue. Observations within this pseudostratified epithelium both *in vivo* and *in vitro* have found that neural progenitors undergo interkinetic nuclear migration (IKNM) between cell divisions[5]. After a period of proliferation, cells exit the cell cycle, differentiate, migrate into the correct radial and lateral positions, and form synapses[20–22]. At this critical step, the mechanical properties which facilitate the neurons' morphogenic movements are unknown as neither the AFM, nor any other conventional technique, allow probing (a) inside 3D tissues (b) at second to hours timescale.

Here, we reveal the mechanical properties which contextualize the neuronal movements of retinogenesis by probing inside living mammalian retina tissue. By combining retina organoids as *in vitro* models for the mammalian retina and magnetic droplets as *in situ* mechanical actuators[23], we were able to measure the time dependent

mechanical properties on timescales from seconds to hours, and carry out mechanical characterizations over multiple days of development.

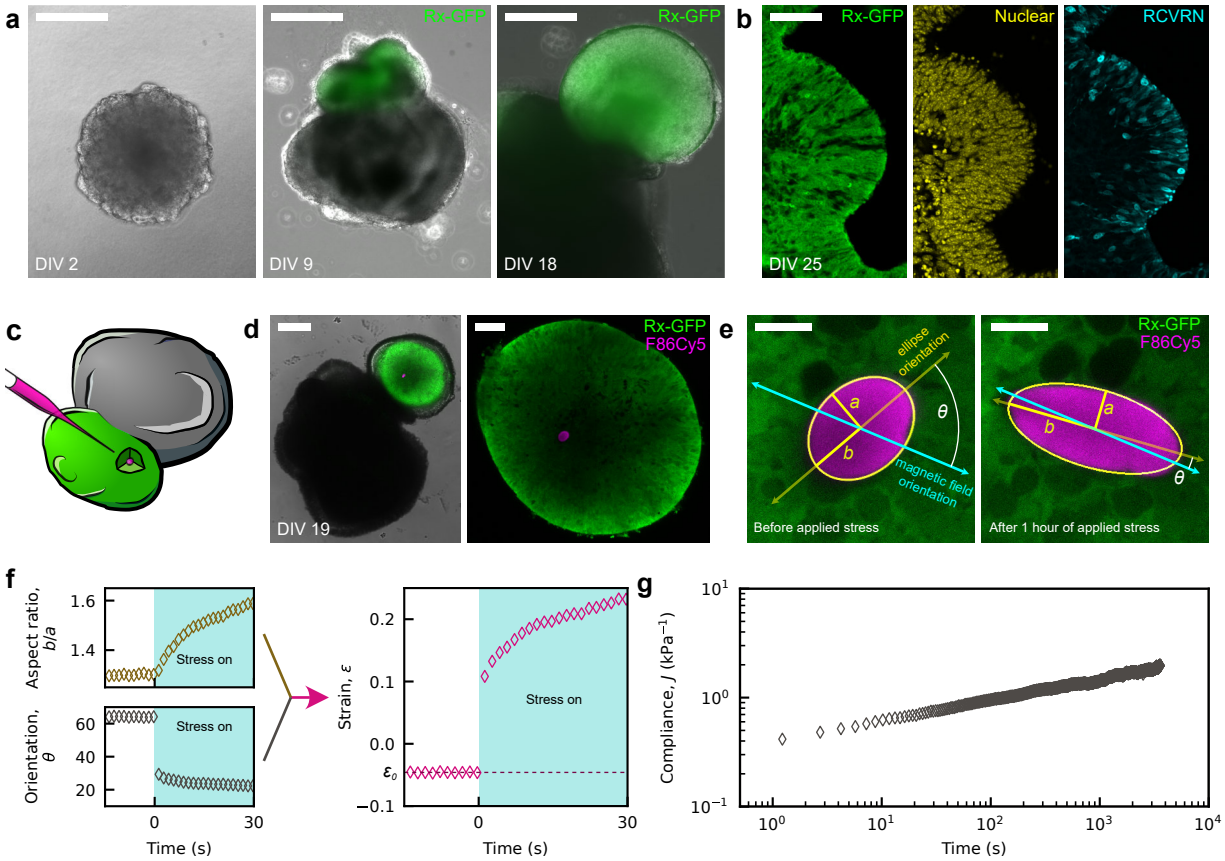

Fig. 1 Probing the mechanics of mammalian retina organoids *in situ* using ferrofluid droplets as mechanical actuators. a, Phase contrast and fluorescence microscopy images of retina organoids grown from mouse embryonic stem cells at days in vitro (DIV) 2, 9, and 18. Retina cells become visible as GFP is expressed under retina promoter Rx at DIV 9 and 18. **b**, Confocal microscopy images of a cryosectioned organoid fixed on DIV 25 showing, left to right, GFP, nuclear stain, and recoverin immunostain (See Suppl. Movie 1). **c**, Sketch showing the injection of fluorescent magnetically responsive oil droplets into retina tissue. **d**, Confocal and transmitted light images of a DIV 19 retina organoid with magnetic droplet after injection. **e**, Confocal microscopy images of droplet (magenta) embedded in retina tissue (green) before (left) and after (right) the onset of applied stress (See Suppl. Movie 2). The elliptical segmentation of the droplet is shown (yellow), with the lengths a and b of the minor and major semi-axes and the relative orientation of the ellipse, θ, with respect to the magnetic field. **f**, Plots of b/a and θ versus time demonstrate how the aspect ratio and orientation change with onset of stress (left). Together, b/a and θ determine the strain ε (right). Dashed line indicates initial strain ε_0. **g**, The compliance $J = (\varepsilon - \varepsilon_0)/\sigma$ is plotted against time for the entire duration of applied stress (1 hour). $\sigma = 371 \pm 12$ Pa (mean $\pm$ s.d., see Methods). Scale bars: **a** 200, **b** 50, **d** 200 (left), 50 (right), **e** 10, all in microns.

2 Results

2.1 Probing long-term mechanics in a mammalian retina organoid

To grow an *in vitro* model of the mammalian retina, we followed an established protocol for generating retina organoids from mouse embryonic stem cells (ESCs) (Fig. 1a; Methods)[14, 24]. The Rx-GFP line provides a fluorescence-based readout for the differentiation into retina cells types as GFP is expressed under the retina tissue specific promoter Rx[14]. We confirmed development of photoreceptor cells by recoverin immunostaining and confocal microscopy imaging in organoids from the first round of culture in which we collected mechanical measurements (Fig. 1b; Suppl. Movie 1, Methods).

We applied a carefully calibrated stress dipole to the retina tissue using magnetically responsive droplets building on our previous experiments in non-neuronal systems[23, 25], as detailed in Methods. Previous implementations of the technology relied on the measurement of the ferrofluid magnetization curve as well as the magnetic field. Both required specialized equipment such as a superconducting quantum interference device (SQUID)[23]. Here, we calibrated the applied stresses purely using Newtonian fluids with known viscosity as a standard, making the technology accessible to other researchers (Methods). To improve analysis, we developed a python-based open source software package for data analysis with a graphical user interface (GUI) and made it available to the community (https://github.com/serwane/retina_mechanics, Methods, Suppl. Fig. 1). To reliably quantify tissue strain along arbitrary directions within the imaging plane we optimized the strain readout and image segmentation (Methods, Suppl. Note 1). Taken together, these improvements allowed us to perform hour-long compliance measurements at high fidelity. We injected droplets with radii between 9 and 26 microns which were both magnetic and fluorescent[26] into retina regions which we identified via the fluorescence signal (Fig. 1c and Methods). Following an injection, we incubated the organoid for several hours and then performed live-imaging (Methods). For each measurement, we confirmed that the droplet was situated inside the thin (up to 100 microns) retina layer (Suppl. Movie 1) using confocal microscopy (Fig. 1d). We collected time series of confocal sections before and during the application of stress (Fig. 1e, Suppl. Movie 2, Methods), and quantified the droplet's aspect ratio b/a and relative orientation θ at every time point using an elliptical segmentation (Fig. 1e,f, Methods). From the aspect ratio and orientation of the droplet we calculated the strain as

$$\varepsilon = \left(\frac{b}{a}\right)^{2/3} \left(\sin^2\theta \left(\frac{b}{a}\right)^2 + \cos^2\theta\right)^{-1/2} - 1 \tag{1}$$

[27]. Since the droplets were strained uniaxially, we obtained the effective tensile creep compliance along an arbitrary direction as

$$J(t) = \frac{\varepsilon(t) - \varepsilon_0}{\sigma}, \tag{2}$$

where ε_0 is the average strain before the application of the magnetic field and σ is the magnitude of the applied magnetic stress introduced at $t = 0$.

To study material properties in the early stages of retina development, we measured $J(t)$ using organoids from three independent experiment rounds and on days in vitro (DIV) ranging from 16 to 24. Within this time period, retina progenitor cells differentiate into the major cell types, including ganglion cells, horizontal cells, cones, amacrine cells, rods, and bipolar cells[17]. The retina becomes laminated, organizing the different neurons into distinct layers. DIV 20 corresponds to the day of birth of the mouse[17].

2.2 Retina tissue remodels in a scale-free manner

We applied stresses and measured the compliance for a duration of up to 1 hour with a temporal resolution of 1.5 seconds (Fig. 1j). One intriguing finding is that, when forces are applied within the retina tissue, the creep compliance shows a scale-free behaviour across 4 orders of magnitude. We found this power law scaling with respect to time for all our measurements across organoid days and rounds (Fig 2a). The quality of the power law fit is excellent, with R^2 values above 0.95 for 15 of 16 measurements (Fig. 2a, Methods). To model such a system using a simplistic mechanical circuit we used a single fractional-order linear viscoelastic element called a springpot[28]. The springpot is fully described by just two parameters, β and c_β, and provides the creep compliance as[29]

$$J(t) = \frac{1}{c_\beta \, \Gamma\left(1+\beta\right)} \, t^\beta \tag{3}$$

where Γ is the Gamma-function. The dimensionless scaling exponent β tunes the response of the element from purely elastic, $\beta = 0$, to purely fluid, $\beta = 1$, with intermediate values describing the relative fluidity of the viscoelastic response. The parameter c_β has units of Pa·s$^\beta$, reflecting the magnitude of viscoelastic resistance to displacement and flow. From fittings to the compliance data (Methods), we found $\beta = 0.14 \pm 0.05$ (mean $\pm$ s.d.) and $c_\beta = 1.52^{+1.06}_{-0.63}$ kPa·s$^{\bar{\beta}}$ (geometric mean, geometric s.d.). These values for β demonstrate that the retina tissue, while still viscoelastic, is more solid-like than fluid-like (Fig. 2b).

The elegance of the springpot model is that it provides analytical solutions for the frequency dependence of the effective tensile storage and loss modulus. This allow us to calculate their magnitude from the experimentally determined values of β and c_β at various frequencies (Fig. 2c). Since $\beta < 0.5$, the storage modulus always dominates over the loss modulus (Fig. 2c), highlighting the elastic behaviour. We find a scaling of the tensile storage and loss modulus as $E' \propto \omega^\beta$ and $E'' \propto \omega^\beta$, respectively. This scaling behaviour together with the magnitude of β are consistent with the properties of a soft glassy material above the glass transition as discussed by Sollich and coauthors[30].

2.3 Quantifying mechanics on the timescales of retinogenesis

We quantified the effective Young's modulus and viscosity of the neurons' environment at the scales relevant to retinogenesis, including the time and length scales of interkinetic nuclear migration, cell division, and differentiation as depicted in Fig. 3a. From

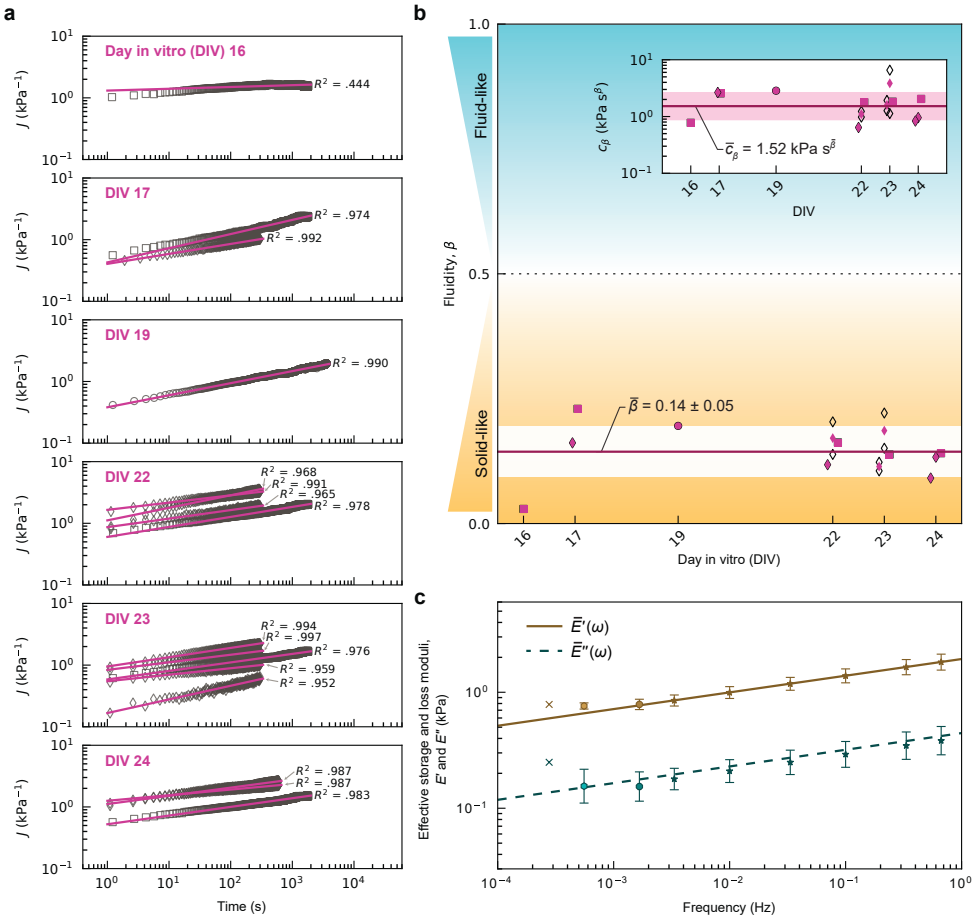

Fig. 2 Scale invariance of strain relaxation in developing mammalian retina. a, Creep compliance in the retina tissue of mouse organoids ranging from DIV 16 to 24 are plotted against time. Lines show power law fits to data using equation 3 (Methods). **b**, The scaling exponents β obtained from (a) plotted against DIV remain smaller than 0.5, indicating solid-like behaviour. Inset: c_β plotted against DIV indicating the magnitude of viscoelastic resistance to the actuation. In **a** and **b**, measurements from different rounds of culture are plotted with different shapes (diamond, square, or circle). In the diamond round, pairs of compliance measurements were taken for organoids on DIV 22 and 23. These paired measurements are plotted in empty markers, and the average of these values is plotted in a filled marker. Lines indicate average values across all organoids, and the bands indicate ± one standard deviation of the mean. For $\bar{c}_\beta$, the geometric mean and standard deviation were used. **c**, The effective tensile storage modulus $\bar{E}'(\omega) = \bar{c}_\beta \omega^{\bar{\beta}} \cos(\frac{\pi}{2}\bar{\beta})$ (solid line) and loss modulus $E''(\omega) = \bar{c}_\beta \omega^{\bar{\beta}} \sin(\frac{\pi}{2}\bar{\beta})$ (dashed line) extrapolated across a range of frequencies. For select frequencies, the geometric average storage and loss moduli are plotted. The marker shape (x, $n = 1$; hexagon, $n = 6$; octogon, $n = 8$; star, $n = 13$.) indicates number of organoids n represented in the data point. Each geometric average computed at frequency f reflects all measurements in which the maximal observation time $t_{\max} \geq 1/f$. Error bars indicate geometric standard error of the mean.

the effective tensile storage and loss modulus, we calculated the Young's modulus, E, and dynamic viscosity, η, for timescales $\tau = 2\pi/\omega$ from 1 to 10^4 seconds. (Fig. 3b,c, Methods). Evaluated at the timescale of one second, we found the geometric average of Young's moduli across all organoids to be $0.80^{+0.64}_{-0.36}$ kPa, in excellent agreement with values obtained from the bulk modulus of the guinea pig and the mouse retina determined via the AFM[6, 10].

Based on the springpot model, the Young's modulus scales as $E \propto \tau^{-\beta}$. Using the experimentally determined values for β and c_β we found the elastic modulus decreases to $0.21^{+0.09}_{-0.06}$ kPa at 10^4 seconds. Thus, the tissue becomes softer. For small values of β, the viscosity shows a much stronger timescale dependence, scaling as $\tau^{1-\beta}$, implying an increase from $9.0^{+16.2}_{-5.8}$ Pa·s at 1 second to 24^{+20}_{-11} kPa·s at 10^4 seconds. The tissue becomes effectively more viscous for longer observation times which might directly affect the ability of neurons to navigate their micro-environment to reach their final destination.

3 Discussion

For technical and ethical reasons, human embryonic development is largely inaccessible to state of the art mechanobiological tools, and many of these same challenges apply to non-human mammalian systems. The combination of neural organoid culture and *in situ* mechanical probing using magnetic droplets allowed us to quantify the time-dependent mechanical properties that govern the shaping of retina tissue during development in a way that overcomes the major challenges associated with human and non-human mammalian systems.

For a long time, researchers have recognized the importance of time-dependence in material properties. Our measurements show that, from one second to one hour, retina cells are navigating an effective Young's modulus which decreases by a factor of four while the effective dynamic viscosity increases by more than three orders of magnitude. How time-dependent material properties affect neuronal network formation remains an open question. *In vivo* experiments in Xenopus have shown that axon growth is controlled by the stiffness of the environment at a Young's modulus of about 0.6 kPa characterized at seconds timescale[1]. At the same time, cell culture experiments have indicated that the formation of synapses typically takes minutes to hours[31]. This work opens a new avenue of mechanobiology research by exploring the role of time-dependent material properties in neurogenesis[21].

Power-law scaling of the creep response as well as the storage and loss modulus demonstrates that the constitutive relations of complex neuronal tissues can be captured by elegant models. We are able to describe tissue compliance across four orders of magnitudes with a single parameter outperforming traditional viscoelastic models in simplicity[28]. Dashpot-spring models require at least four additional model parameters and fail to describe the experimental data in the limit of short and long timescales (Suppl. Figure 4). The observed scaling implies that the material has no particular intrinsic timescales at which stresses are relaxed, rather a continuum of relaxation modes. At the same time, as it is unclear where this simple scaling comes

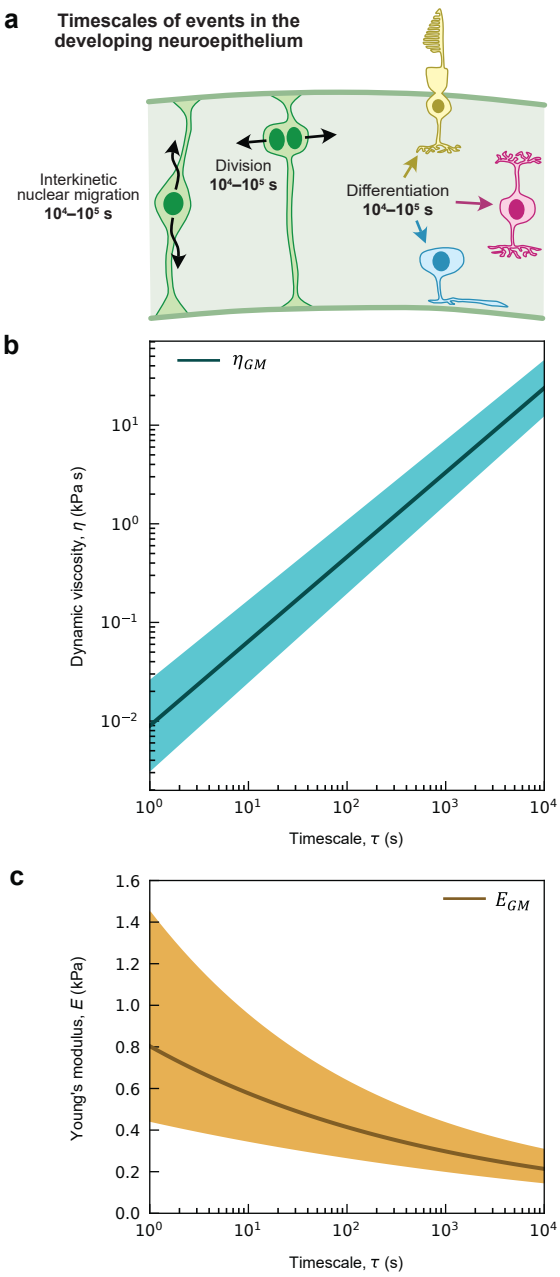

Fig. 3 Quantifying the mechanics of the cellular mircoenvironment during retina development. a, The development of neuroepithelial tissues, like the retina, requires force-driven nuclear and cellular rearrangements to transform from a pseudo-stratified epithelium into a laminated structure of different cell types[20, 21]. **b**, The dynamic viscosity $\eta = \frac{5}{36}E''$ and **c**, Young's modulus $E = \frac{5}{12}E'$calculated from data in Figure 2 as a function of timescale $\tau = 2\pi/\omega$. Lines indicate geometric means η_{GM} and E_{GM}. Bands indicate geometric standard deviation. $n = 13$ organoids.

from, we would like to understand what physical and biological mechanisms underlie this scale-free remodelling and how they connect to retina formation and function.

Our measurements inspires us to think of the forming retina as an amorphous material near the glass transition. Indications of soft glassy rheology (SGR) have been shown via the recording of cell dynamics in 2D cell culture[32] and in 3D in non-neuronal embryonic tissues[33]. One mechanical hallmark of SGR is the power law scaling of storage and loss modulus as a function of frequency[30, 34]. We measured a scaling of the storage and loss modulus as ω^β with $\beta = 0.14$ which is consistent with a soft glassy material near and above the glass transition[30]. We recapitulate findings in 2D cell culture where power law scaling at subcellular scale has been reported[34–36]. Magnetic tweezer experiments on the cytoskeleton of various cell lines found $\beta \in [0.17, 0.25]$[34, 35, 37] which is comparable with the value which we report here at completely different length and time scales, for 3D neuronal tissue. Future experiments will reveal whether a caging-uncaging behaviour can be observed in retina organoids. We hypothesize that a glassy material near and above its glass transition is a way to balance the competing engineering goals of retina development: maximizing retina imaging resolution requires a dense, regular packing of neurons; at the same time, tissue growth necessitates the dynamic refinement of the architecture. We observe a relatively small spread in the measurements of the scaling exponent β (Fig. 2b). We speculate that β might be a tightly regulated physical property of the tissue, even in the presence of relatively large heterogeneities in absolute stiffness in various biological replicates. Whether the scaling behaviour is reminiscent only of retina tissue or a general hallmark of other neuronal systems is an open question which could be explored by applying the concepts presented here in other organoid systems including cerebral human organoids.

In non-neuronal tissues, a transition from a fluid-like to a solid-like state has been observed as a mechanical mechanism underlying development[25, 38, 39]. For epithelial sheets, a jamming-unjamming transition has been well captured by vertex models[40, 41]. Recent theoretical work has predicted different power law exponents for storage and loss modulus as a function of excitation frequency ω depending on the jammed and unjammed state[41]. In contrast, our measurements revealed a scaling of both storage and loss modulus with ω^β. Whether the rheologies simulated in 3D vertex models show scalings similar to our measurements is an open question. Non-mammalian retina development has been described in the framework of a jamming-unjamming transition based on imaging of tissue architecture and cell nuclei[42]. We believe our approach allows for a direct experimental determination of the constitutive relation, not only in developing tissues but in a broader context of soft matter systems, including tunable hydrogels[43].

4 Methods

Stem cell culture and retina organoid generation

We generated organoids from mouse embryonic stem cells in three independent rounds. For each round, we thawed Rx-GFP K/I EB5 cells (AES0145, RIKEN) from LN2 storage at passages 26, 23, and 23, respectively, and maintained them for two

passages according to a previously published protocol[14, 24] prior to retina differentiation. We seeded 3×10^3 cells per well in 100 µl volumes in 96-well round bottom plates on DIV 0 and added 2 % Matrigel on DIV 1. We cultured organoids at 20 % O_2 until DIV 7, before transferring to Petri dishes for further culture in retina maturation medium 1 at 40 % O_2. On DIV 10, we transferred organoids to new dishes containing retina maintenance media 2 (RMM2). We supplemented RMM2 with 0.5 µM EC23 from DIV 10-14 and with 1 mM taurine from DIV 10. On DIV 14, we screened retina organoids for GFP under a Nikon SMZ25 stereoscope with a 0.5X SHR Plan Apo objective and fluorescence illumination and transferred GFP-positive organoids intact (without trisection) to new dishes with fresh media. We maintained organoids up to DIV 26, removing and replacing half of the media on DIV 16, 18, 21, 23, and 25.

Immunohistochemistry

A selection of organoids from the first round of culture in which we made mechanical measurements were fixed in 4% PFA for 60 minutes on an orbital shaker at 4°C. Following fixation, organoids were rinsed three times in PBS. After four days in PBS at 4°C, organoids were transferred to 30% sucrose and held overnight at 4°C, before being embedding and frozen in optimal cutting temperature compound. Organoids were cut into 10-30 micron thick sections on a cryotome (CryoStar NX70). Sections were held at 4°C prior to staining. We performed immunohistochemistry using recoverin Rabbit IgG (1:500) and goat anti-rabbit AF568(1:500)(Merck Millipore AB5585). We blocked sections (90% PBST; T = TritonX 0.5% and 10% NGS) for 1 hour at room temperature. Following a PBS rinse, we incubated sections in primary antibody overnight at 4ºC and in secondary antibody for 4 hours at room temperature, with PBS rinses between and afterwards. Finally, we stained sections with Nucspot650 (Biotium) (1:500) for 30 minutes before a final wash. We mounted sections in FlourmountG on a glass cover slip and stored samples at 4° C.

Preparation and injection of ferrofluid

We prepared magnetic oil for injection experiments from a 1:1 (v/v) mixture of 0.2 micron filtered DFF2 (Ferrotec) and Fluorinert FC40 (FL-005-HP-1000, 3M) with 2.5 weight % 008-FluoroSurfactant (RAN Biotechnologies) and 250 µM F86Cy5[26]. To control the concentration of DFF2 across multiple rounds and to compensate evaporation, we stored the magnetic oil at 4 C and thinned it with Fluorinert FC40 as needed. Prior to injection, we sonicated the magnetic oil for 10 minutes at room temperature before loading it into a 55 mm long straight spiked 10 micron ID ICSI-Pipette (BM100T-10P, BioMedical Instruments).

We injected organoids with ferrofluid droplets under a Nikon SMZ25 stereoscope (see above) on agarose under RMM2 media. Immediately after organoid injection, we injected ferrofluid into N190000 viscous standards (Cannon Instrument Company) to calibrate the applied stress (Suppl. Information).

Imaging of living and fixed organoids

Prior to injection, we acquired fluorescence and phase contrast images in Fig. 1a using

a Ximea xiC camera mounted to a Zeiss Axiovert 200M inverted fluorescence microscope with condenser. After droplet injection, we maintained organoids at 37°C in a humidified 5% CO_2 40% O_2 environment for approximately 4 hours. For live imaging, we placed organoids within a silicone well sandwiched between two glass coverslips and filled with supplemented RMM2 before transferring to the 37°C live imaging chamber (Digital Pixel). We performed all confocal microscopy on a Zeiss LSM 980. We imaged the fixed section in Fig. 1b with a C-Achroplan 32x/0.85 water immersion objective. We imaged droplets in stress calibration measurements in viscous standards with the A-Plan 10x/0.25 air objective and the droplets for mechanical measurements in organoids with either the Plan-Apochromat 20x/0.8 M27 air objective or the LD LCI Plan-Apochromat 40x/1.2 Imm Korr DIC M27 objective. We acquired all time series at a rate of 1 frame per 1.5 seconds and frame scan time of 0.2 seconds. To improve visibility for the reader in Fig. 1e, we used Fiji to sum images from a mechanical measurement time series (DIV 19, Fig. 1f,g and Fig. 2a) across 10 frames.

Application of magnetic stress

We applied a step change in stress to the magnetic droplet by rapidly moving a Hallbach array of permanent magnets mounted to a LabVIEW controlled linear stage, as previously described[23], from an initial position far from the droplet (low stress, $\sigma_m = \sigma_0$) to a final position close to the droplet (high stress, $\sigma_m = \sigma_0 + \sigma$), while imaging the droplet with confocal microscopy. In order to determine the orientation, timing, and magnitude of the applied stress in the organoid, we applied the *same* magnetic field to droplets in viscous standards (N190000, Cannon Instrument Company) at 37 ± 0.1 C.

Calculation of strain

In the absence of other stresses, the droplet strain under a uniaxial stress is $\varepsilon = (b/a)^{2/3} - 1$. When other stresses may be present in the tissue, the droplet shows a non-zero initial deformation. To calculate the strain in the direction of the applied field in the presence of pre-deformations we use the droplet's aspect ratio b/a and declination, θ, relative to the magnetic field (Figure 1e). We measured the magnetic field orientation from the alignment of the elliptical segmentation of the droplet at maximal strain in calibration measurements. Following the example of [27], it can be shown that the angle-corrected strain along an arbitrary axis is given by $\varepsilon = \left(\frac{b}{a}\right)^{2/3} \left(\sin^2\theta \left(\frac{b}{a}\right)^2 + \cos^2\theta\right)^{-1/2} - 1$. A full derivation can be found in Suppl. Note 1.

A python-based user-friendly interface for droplet shape analysis and fitting

To be able to perform calibrations, image processing and analysis efficiently on long time series we developed a python-based user interface using libraries like NumPy, SciPy, and OpenCV. The pipeline consists of three main tabs - analyzing, calibrating, and fitting. For a screenshot, see Suppl. Fig. 1. The graphical user interface (GUI) allows users to fit ellipses to droplet images from time-lapse sequences. This process generates strain curves, which are used in a next step to extract the material's

mechanical properties. The software is programmed in a modular way using separate classes for the GUI, image analysis, and fitting algorithms. The fitting algorithm uses the `curve_fit` function from `SciPy`[44] to model pre-magnetic and the magnetic field phase (creep). The best fit is selected based on minimal residuals by iterating 100 times over statistically varied initial conditions. The pipeline also features error propagation using the `uncertainties`[45] package, providing uncertainty estimations for fit parameters. A calibration measurement routine ensures the accuracy of the applied stress by accounting for experimental errors, including fitting errors and errors in the measurement of the viscous standards.

Modeling organoid mechanics

We modelled the mechanical response of the droplet in the organoid as a single springpot element characterized by the two parameters β and c_β giving the creep compliance $J(t) = \frac{1}{c_\beta \Gamma(1+\beta)} t^\beta$. We obtained β and c_β from a linear fit to the log transformed time and compliance data. In contrast to the Kelvin-Voigt model used for calibration measurements, our model for the strain dynamics in the organoid does not consider the droplet capillary forces as a parallel spring element, as we could not observe any stiffening effect on the long term behaviour of the creep compliance. See Suppl. Fig. 3 for a comparison between the single springpot model and a springpot in parallel with a spring. While other models were considered (see Suppl. Fig. 4), the springpot is the simplest model for describing the data. We obtained values for the Young's modulus and dynamic modulus from the parameters of the springpot model (β and c_β) following the example of [28], and applying numerical factors to relate the 1D tensile storage and loss modulus to the 3D Young's modulus and dynamic viscosity, as was done previously[23].

Calibration of applied stress

To determine precisely how much stress was applied during a measurement in organoid tissue, for each day of organoid measurements we injected multiple droplets (typical diameters 85 ± 35 microns) of the same magnetic oil used in the organoid into a viscous standard (N190000, Lot no. 14101d, Cannon Instrument Company). To control the viscosity, the imaging chamber and sample were held at $(37.0 \pm 0.1)^\circ$C while calibration experiments were performed. We acquired fluorescence confocal time series of the droplet (1.5 second interval time) while introducing a magnetic stress, as described above, in the same manner as in the organoid. From these image series, we obtained strain versus time curves using our custom python-based GUI. We determined the magnitude of stress change σ and the time t_0 corresponding to the change by modelling the droplet in viscous standard as a 1D Kelvin-Voigt material with spring k_d and dashpot μ, as before[23]. In this 1D description, the magnetic stress reads $\sigma_\mathrm{m} = k_\mathrm{d}\varepsilon$ where ε is the equilibrium droplet strain and the droplet spring constant $k_d = \frac{6\gamma}{R}$[23, 46, 47]. Under a step change in stress from σ_0 to $\sigma_0 + \sigma$, we model the strain dynamics $\varepsilon(t) = \varepsilon_\Delta \left(1 - e^{-(t-t_0)/\tau}\right) + \varepsilon_0$, where t_0 is when the step change occurs, ε_0 is the initial strain before t_0, $\varepsilon_\Delta + \varepsilon_0$ is the final strain at equilibrium, and $\tau = 6\eta R/5\gamma$ is the relaxation timescale set by the surrounding medium's viscosity (η), the droplet radius (R), and the interfacial tension (γ)[48]. The timescale in our

1D model $\tau = \mu/k_\mathrm{d}$ gives us the relationship between the dashpot μ and dynamic viscosity η as $\mu = (36/5)\eta$. We obtained values for τ, t_0, and ε_Δ by directly fitting the strain versus time data, and we measured the viscosity of N190000 at 37°C to be $\eta_R = (214.5 \pm 6.8)$ Pa s (mean ± s.e.m.) using a rheometer (see Methods below), allowing us to measure k_d and σ.

Compared to the rheometer data, the droplet technique shows very good agreement for materials with viscosities higher than those used for calibration; for example, testing with the Cannon Instrument Company N2700000 viscosity standard results in relative error $\frac{\bar{\Delta}_w}{\bar{\sigma}_w}$ of 4.3% (see Suppl. Fig. 2), where $\bar{\sigma}_w = \frac{\sum_i \frac{\sigma_i}{\Delta_i{}^2}}{\sum_i \frac{1}{\Delta_i{}^2}}$ is the weighted mean stress and $\bar{\Delta}_w$ is the weighted standard deviation were calculated as $\bar{\sigma}_w = \frac{\sum_i \frac{\sigma_i}{\Delta_i{}^2}}{\sum_i \frac{1}{\Delta_i{}^2}}$ and $\bar{\Delta}_w = \frac{1}{\sqrt{\sum_i \frac{1}{\Delta_i{}^2}}}$. The total error of the applied stress $\bar{\Delta}$ contains also the systematic error of the viscosity standard using $\bar{\Delta} = \sqrt{\bar{\Delta}_w^2 + \Delta_\eta{}^2}$, were $\Delta_\eta = \frac{\delta_\eta}{\eta}\,\bar{\sigma}_w$. When calibrating with N190000 at 37°C, the uncertainty in the viscosity from the rheometer measurement ($\delta_\eta/\eta = 3.2\%$) is usually the largest source of error. When considering uncertainties from the fit as well, a typical total relative error in the applied stress amounts to $\bar{\Delta}/\bar{\sigma}_w = 3.4\%$.

Rheometer measurements

The dynamic viscosity η_R of the viscous standards (Cannon Instrument Company) was determined using a shear plate rheometer (Kinexus Ultra+). We first performed frequency and amplitude sweeps to determine the range of frequencies and strains, respectively, where the viscosity remained constant. Then we performed the measurements at a constant frequency and strain that were 10 % smaller than the upper limits of these ranges. For each viscous standard we performed 3–5 measurements at 37°C that lasted between 485–515 seconds. Of each data set, the last data point was dropped and the remaining last 20 data points were averaged to obtain η_R. To test that this method yields accurate results of the standards' viscosities, we also probed the standards N62000 and N190000 at 25°C to compare the results with the values given by the standards' manufacturer for the lots used (Suppl. Table 1).

Acknowledgements. We thank Timo Betz and Max Bi for stimulating discussions. We thank Ellen Sletten for providing the fluorinated dye. We thank Mythili Padavu, Georgii Volkov, Teresa Rogler, Vlasta Hadalin and Lena Glanz for support with the organoid culture. We thank Max Bi and Marie Lackmann for feedback on the manuscript. We thank Joachim Rädler for his support. This work was supported by the European Research Council (ERC) under the European Union's Horizon 2020 research and innovation program (Grant Agreement No. 850691), the Center for NanoScience (CeNS) at the Ludwig-Maximilians-University (LMU), Munich, and the Munich Cluster for Systems Neurology (SyNergy). The work was supported by the Human Frontier Science Program (Grant No. 18807).

Declarations

Data availability. Microscopy data reported in this paper will be shared by the lead contact upon request. Any additional information required to reanalyze the data reported in this paper is available from the lead contact upon request.

Materials availability. No plasmids were generated in this study.

Code availability. The python code for analysis can be accessed at https://github.com/serwane/retina_mechanics.

Author contribution. E.R.S and F.S. conceived the research. R.J. cultured the mouse retina organoids. M.F., E.R.S and F.S. developed the analysis pipeline. E.R.S, M.F. and A.T.B. analyzed the data. Droplet injection experiments and confocal imaging was performed by E.R.S. and M.F. Viscous standards were probed on the rheometer by A.T.B. and F.S.. Immunohistochemistry was performed by R.J. Statistical analysis was performed by E.R.S. All authors contributed to the manuscript.

References

[1] Koser, D. E. *et al.* Mechanosensing is critical for axon growth in the developing brain. *Nature Neuroscience* **19**, 1592–1598 (2016). http://dx.doi.org/10.1038/nn.4394.

[2] Llinares-Benadero, C. & Borrell, V. Deconstructing cortical folding: genetic, cellular and mechanical determinants. *Nature Reviews Neuroscience* **20**, 161–176 (2019). http://dx.doi.org/10.1038/s41583-018-0112-2.

[3] Pillai, E. K. & Franze, K. Mechanics in the nervous system: From development to disease. *Neuron* **112**, 342–361 (2024). http://dx.doi.org/10.1016/j.neuron.2023.10.005.

[4] Yanakieva, I., Erzberger, A., Matejčić, M., Modes, C. D. & Norden, C. Cell and tissue morphology determine actin-dependent nuclear migration mechanisms in neuroepithelia. *Journal of Cell Biology* **218**, 3272–3289 (2019). http://dx.doi.org/10.1083/jcb.201901077.

[5] Rocha-Martins, M. *et al.* Neuronal migration prevents spatial competition in retinal morphogenesis. *Nature* **620**, 615–624 (2023). http://dx.doi.org/10.1038/s41586-023-06392-y.

[6] Franze, K. *et al.* Spatial mapping of the mechanical properties of the living retina using scanning force microscopy. *Soft Matter* **7**, 3147 (2011). http://dx.doi.org/10.1039/C0SM01017K.

[7] Weber, I. P., Yun, S. H., Scarcelli, G. & Franze, K. The role of cell body density in ruminant retina mechanics assessed by atomic force and brillouin microscopy. *Physical Biology* **14**, 065006 (2017). http://dx.doi.org/10.1088/1478-3975/aa6d18.

[8] Ambekar, Y. S. *et al.* Characterization of retinal biomechanical properties using brillouin microscopy. *Journal of Biomedical Optics* **25** (2020). http://dx.doi.org/10.1117/1.jbo.25.9.090502.

[9] Wu, P.-H. *et al.* A comparison of methods to assess cell mechanical properties. *Nature Methods* **15**, 491–498 (2018). http://dx.doi.org/10.1038/s41592-018-0015-1.

[10] Gutmann, M. *et al.* Beyond comparison: Brillouin microscopy and afm-based indentation reveal divergent insights into the mechanical profile of the murine retina. *Journal of Physics: Photonics* **6**, 035020 (2024). http://dx.doi.org/10.1088/2515-7647/ad5ae3.

[11] Lee, S. *et al.* Measurement of viscoelastic properties in multiple anatomical regions of acute rat brain tissue slices. *Journal of the Mechanical Behavior of Biomedical Materials* **29**, 213–224 (2014). http://dx.doi.org/10.1016/j.jmbbm.2013.08.026.

[12] Budday, S., Ovaert, T. C., Holzapfel, G. A., Steinmann, P. & Kuhl, E. Fifty shades of brain: A review on the mechanical testing and modeling of brain tissue. *Archives of Computational Methods in Engineering* **27**, 1187–1230 (2019). http://dx.doi.org/10.1007/s11831-019-09352-w.

[13] O'Hara-Wright, M. & Gonzalez-Cordero, A. Retinal organoids: a window into human retinal development. *Development* **147** (2020). http://dx.doi.org/10.1242/dev.189746.

[14] Eiraku, M. *et al.* Self-organizing optic-cup morphogenesis in three-dimensional culture. *Nature* **472**, 51–56 (2011). http://dx.doi.org/10.1038/nature09941.

[15] Nakano, T. *et al.* Self-formation of optic cups and storable stratified neural retina from human escs. *Cell Stem Cell* **10**, 771–785 (2012). http://dx.doi.org/10.1016/j.stem.2012.05.009.

[16] Cowan, C. S. *et al.* Cell types of the human retina and its organoids at single-cell resolution. *Cell* **182**, 1623–1640.e34 (2020). http://dx.doi.org/10.1016/j.cell.2020.08.013.

[17] Llonch, S., Carido, M. & Ader, M. Organoid technology for retinal repair. *Developmental Biology* **433**, 132–143 (2018). http://dx.doi.org/10.1016/j.ydbio.2017.09.028.

[18] Okuda, S. *et al.* Strain-triggered mechanical feedback in self-organizing optic-cup morphogenesis. *Science Advances* **4** (2018). http://dx.doi.org/10.1126/sciadv.aau1354.

[19] Salbaum, K. A., Shelton, E. R. & Serwane, F. Retina organoids: Window into the biophysics of neuronal systems. *Biophysics Reviews* **3** (2022). http://dx.doi.org/10.1063/5.0077014.

[20] Baye, L. M. & Link, B. A. Interkinetic nuclear migration and the selection of neurogenic cell divisions during vertebrate retinogenesis. *The Journal of Neuroscience* **27**, 10143–10152 (2007). http://dx.doi.org/10.1523/jneurosci.2754-07.2007.

[21] Amini, R., Rocha-Martins, M. & Norden, C. Neuronal migration and lamination in the vertebrate retina. *Frontiers in Neuroscience* **11** (2018). http://dx.doi.org/10.3389/fnins.2017.00742.

[22] Lagnado, L. & Schmitz, F. Ribbon synapses and visual processing in the retina. *Annual Review of Vision Science* **1**, 235–262 (2015). http://dx.doi.org/10.1146/annurev-vision-082114-035709.

[23] Serwane, F. *et al.* In vivo quantification of spatially varying mechanical properties in developing tissues. *Nature Methods* (2017).

[24] Völkner, M. *et al.* Retinal organoids from pluripotent stem cells efficiently recapitulate retinogenesis. *Stem Cell Reports* **6**, 525–538 (2016). http://dx.doi.org/10.1016/j.stemcr.2016.03.001.

[25] Mongera, A. *et al.* A fluid-to-solid jamming transition underlies vertebrate body axis elongation. *Nature* **561**, 401–405 (2018). http://dx.doi.org/10.1038/s41586-018-0479-2.

[26] Lim, I. *et al.* Fluorous soluble cyanine dyes for visualizing perfluorocarbons in living systems. *Journal of the American Chemical Society* **142**, 16072–16081 (2020). http://dx.doi.org/10.1021/jacs.0c07761.

[27] Treagus, S. H. Mohr circles for strain, simplified. *Geological Journal* **22**, 119–132 (1987). http://dx.doi.org/10.1002/gj.3350220205.

[28] Bonfanti, A., Kaplan, J. L., Charras, G. & Kabla, A. J. Fractional viscoelastic models for power-law materials. *Soft Matter* (2020).

[29] Paola, M. D. *et al.* Visco-elastic behavior through fractional calculus: An easier method for best fitting experimental results. *Mechanics of Materials* (2011).

[30] Sollich, P., Lequeux, F., Hébraud, P. & Cates, M. E. Rheology of soft glassy materials. *Physical Review Letters* **78**, 2020–2023 (1997). http://dx.doi.org/10.1103/PhysRevLett.78.2020.

[31] Friedman, H. V., Bresler, T., Garner, C. C. & Ziv, N. E. Assembly of new individual excitatory synapses. *Neuron* **27**, 57–69 (2000). http://dx.doi.org/10.1016/S0896-6273(00)00009-X.

[32] Angelini, T. E. *et al.* Glass-like dynamics of collective cell migration. *Proceedings of the National Academy of Sciences* **108**, 4714–4719 (2011). http://dx.doi.org/10.1073/pnas.1010059108.

[33] Schötz, E.-M., Lanio, M., Talbot, J. A. & Manning, M. L. Glassy dynamics in three-dimensional embryonic tissues. *Journal of The Royal Society Interface* **10**, 20130726 (2013). http://dx.doi.org/10.1098/rsif.2013.0726.

[34] Fabry, B. *et al.* Scaling the microrheology of living cells. *Physical Review Letters* (2001).

[35] Fabry, B. *et al.* Time scale and other invariants of integrative mechanical behavior in living cells. *Physical Review E* **68** (2003). http://dx.doi.org/10.1103/PhysRevE.68.041914.

[36] Hurst, S., Vos, B. E., Brandt, M. & Betz, T. Intracellular softening and increased viscoelastic fluidity during division. *Nature Physics* **17**, 1270–1276 (2021). http://dx.doi.org/10.1038/s41567-021-01368-z.

[37] Bonakdar, N. *et al.* Mechanical plasticity of cells. *Nature Materials* **15**, 1090–1094 (2016). http://dx.doi.org/10.1038/NMAT4689.

[38] Petridou, N. I., Grigolon, S., Salbreux, G., Hannezo, E. & Heisenberg, C.-P. Fluidization-mediated tissue spreading by mitotic cell rounding and non-canonical wnt signalling. *Nature Cell Biology* **21**, 169–178 (2018). http://dx.doi.org/10.1038/s41556-018-0247-4.

[39] Atia, L., Fredberg, J. J., Gov, N. S. & Pegoraro, A. F. Are cell jamming and unjamming essential in tissue development? *Cells & Development* **168**, 203727 (2021). http://dx.doi.org/10.1016/j.cdev.2021.203727.

[40] Bi, D., Lopez, J. H., Schwarz, J. M. & Manning, M. L. A density-independent rigidity transition in biological tissues. *Nature Physics* **11**, 1074–1079 (2015). http://dx.doi.org/10.1038/NPHYS3471.

[41] Damavandi, O. K., Arzash, S., Lawson-Keister, E. & Manning, M. L. Universality in the mechanical behavior of vertex models for biological tissues (2022). http://dx.doi.org/10.1101/2022.06.01.494406.

[42] Kim, S. *et al.* A nuclear jamming transition in vertebrate organogenesis. *Nature Materials* (2024). http://dx.doi.org/10.1038/s41563-024-01972-3.

[43] Gharios, R., Francis, R. M. & DeForest, C. A. Chemical and biological engineering strategies to make and modify next-generation hydrogel biomaterials. *Matter* **6**, 4195–4244 (2023). http://dx.doi.org/10.1016/j.matt.2023.10.012.

[44] Virtanen, P. *et al.* SciPy 1.0: Fundamental Algorithms for Scientific Computing in Python. *Nature Methods* **17**, 261–272 (2020).

[45] Lebigot, E. O. Uncertainties: a python package for calculations with uncertainties. Website (2023). Online available: http://pythonhosted.org/uncertainties/; Retrieved June 2023.

[46] Rowghanian, P., Meinhart, C. D. & Campàs, O. Dynamics of ferrofluid drop deformations under spatially uniform magnetic fields. *Journal of Fluid Mechanics* **802**, 245–262 (2016). http://dx.doi.org/10.1017/jfm.2016.447.

[47] Tsebers, A. O. Virial method of investigation of statics and dynamics of drops of magnetizable liquids. *Magnetohydrodynamics (Engl. Transl.); (United States)* **21**, 25–34 (1985). https://www.osti.gov/biblio/5829913.

[48] Rallison, J. M. The deformation of small viscous drops and bubbles in shear flows. *Annual Review of Fluid Mechanics* **16**, 45–66 (1984). http://dx.doi.org/10.1146/annurev.fl.16.010184.000401.